Journal of Electrical and Electronics Engineering (IOSR-JEEE)
e-ISSN: 2278-1676, p-ISSN: 2320-3331, Volume 21, Issue 4 Ser. 1 (July. – August. 2026), PP 35-49
www.iosrjournals.org

The Behavior Of The Output Fields Of A Helical Rectangular Waveguide With Alternating Circular Dielectric And Hollow Layers

Zion Menachem
Department Of Electrical Engineering, Sami Shamoon College Of Engineering, Beer Sheva, Israel

Abstract
This research presents a method for computing electromagnetic field propagation in a rectangular helical waveguide whose cross-section consists of alternating circular dielectric and hollow layers. The main goal of this study is to examine the behavior of the output fields in this interesting and challenging case. The helical geometry is described using a coordinate transformation involving two rotations and a translation, parameterized by the cylinder radius R and helix angle δ_p. Traditional analytical methods struggle with inhomogeneous cross-sections in straight and bent waveguides that include many different layers. We employ a helical waveguide model, and develop the proposed technique for solving the specific geometry of the cross-section. The proposed technique will enable a solution of a complex bending problem that cannot be solved by traditional analytical methods. In this study, we examine the influence on the output fields of this curved waveguide in three-dimensional space with a specific cross section composed of alternating circular dielectric and hollow layers. The proposed technique will be most useful for the examination of helical waveguides with a cross section composed of a large number of circular dielectric layers, particularly for advanced systems with helical waveguides comprising multiple circular dielectric and hollow layers operating in the microwave regime.
Keywords: *Wave propagation, helical waveguide, helix angle, dielectric and hollow layers, rectangular waveguide.*

Date of Submission: 16-07-2026 Date of Acceptance: 26-07-2026

I. Introduction

Research interest in the field of curved waveguides and dielectric materials has seen significant growth in the last years. The propagation constant modes were determined for a hollow circular waveguide in [1]. The bending losses of an infrared metallic waveguide were studied with mode-coupling analysis in [2]. A general method was developed in [3] to evaluate the propagation constant in circular hollow-core waveguides. An effective analysis technique for curved waveguides with a dielectric and a hollow layer was presented in [4]. In [5], a bent mode in dielectric waveguide was discussed, while an analysis of bending losses in dielectric layers was proposed in [6]. In [7], an analytic method for dielectric optical slab waveguides was proposed, while in [8] a curved waveguide by using the finite-difference method was proposed. Ultra-compact and efficient photonic waveguide bends were proposed in [9], and a hollow waveguide with a graded multilayered dielectric medium was proposed in [10].

A curved waveguide with direct laser writing in polymer was proposed in [11], and a teraherz circular dielectric waveguide was presented in [12]. The authors in [13] proposed a model for waveguides with angled and curved dielectric interfaces. The propagation of fields within a nanomaterial graphene in slab waveguide was published in [14]. The propagation in slab waveguides was proposed in [15]. Another curved waveguide with laser beam was proposed in [16], while in [17], the design of a large curved waveguide for the application of graded photonic crystal was given. A curved GaAs cantilever waveguide for photonic integrated circuits was proposed in [18]. Field propagation in a helical waveguide was given in [19], and in [20], the computation of the fields in curved rectangular waveguide was given. Propagation in curved waveguide was proposed in [21]. A direct near-field observation of conversion between waveguide modes and leaky modes in periodic structure was given in [22]. The development of a waveguide for periodic layers was presented in [23]. Lastly, a periodic waveguide with arbitrary shaped corrugation was proposed in [24], and in [25], Bloch modes were characterized in an optical waveguide.

In this research we will examine the influence on the output field of a helical waveguide with a specific cross section composed of several circular dielectric and hollow layers. We will use the method for curved waveguides [4] for the specific cross section, as shown in Fig. 1(b). The proposed technique makes an important contribution to the solution of wave propagation in a helical waveguide with an inhomogeneous cross section composed of several circular dielectric and hollow layers. The proposed technique is very important, especially where the cross section of the helical waveguide composed of a large number of circular dielectric layers. The whole paper is organized as follows. In the next section we present the helical waveguide with the specific rectangular cross section. The proposed model for the helical waveguide and the technique for solving the cross section is given in the third section. The numerical results are given in the fourth section, and the conclusions are presented in the last section.

II. Helical Waveguide With The Specific Rectangular Cross Section

The helical transformation of the Cartesian coordinates is achieved by two rotations and one translation, and is given in the form:

$$\begin{pmatrix} X \\ Y \\ Z \end{pmatrix} = \begin{pmatrix} cos(\phi_c) & -sin(\phi_c) & 0 \\ sin(\phi_c) & cos(\phi_c) & 0 \\ 0 & 0 & 1 \end{pmatrix} \begin{pmatrix} 1 & 0 & 0 \\ 0 & cos(\delta_p) & -sin(\delta_p) \\ 0 & sin(\delta_p) & cos(\delta_p) \end{pmatrix} \begin{pmatrix} r\sin\theta \\ 0 \\ r\cos\theta \end{pmatrix} + \begin{pmatrix} Rcos(\phi_c) \\ Rsin(\phi_c) \\ \zeta sin(\delta_p) \end{pmatrix}, \quad (1(a,b,c))$$

where ζ is the coordinate along the helix axis, R is the radius of the cylinder, δ_p is the helix angle, and $\phi_c = (\zeta\cos(\delta_p))/R$. The radius of the cylinder of the helical waveguide is given by $R = (\zeta\cos(\delta_p))/(\phi_c)$.

The metric coefficients in the case of the helical waveguide in accordance with Eqs. (1a)-(1c) are:

$$h_x = 1, \quad (2a)$$

$$h_y = 1, \quad (2b)$$

$$h_\zeta = \sqrt{(1+\frac{x}{R})^2 \cos^2(\delta_p) + \sin^2(\delta_p)(1+\frac{y^2}{R^2}\cos^2(\delta_p))}$$

$$= \sqrt{1+\frac{2x}{R}\cos^2(\delta_p) + \frac{x^2}{R^2}\cos^2(\delta_p) + \frac{y^2}{R^2}\cos^2(\delta_p)\sin^2(\delta_p)}$$

$$\simeq 1 + \frac{x}{R}\cos^2(\delta_p). \quad (2c)$$

Figure 1(a) shows the helical waveguide and Fig. 1(b) shows the specific rectangular cross section. The axes and the coordinate along the helix axis (ζ) are shown in Fig. 1(c). The parameter ζ is the coordinate along the helix axis, and R is the cylinder radius. The deployment of the helix is shown in Fig. 1(d), where δ_p is the helix angle, and ϕ_c is the peripheral angle, where $0 \le \phi_c \le 2\pi$ and $\phi_c = (\zeta/R)\cos(\delta_p)$.

This research introduces a method to analyze rectangular helical waveguides with a periodic structure in the cross section, bounded by a dielectric material and metal. The cross section (Fig. 1(b)) shows a periodic structure of four circular dielectric and hollow layers. Medium 1 consists of a circular hollow layer in the core, medium 2 consists of a circular dielectric layer, medium 3 consists of a circular hollow layer and medium 4 consists of a circular dielectric layer. The thickness of the two circular dielectric layers shown in Fig. 1(b) are given by d_1=r_2-r_1, d_2=r_4-r_3, where $r_4 > r_3 > r_2 > r_1$. The dielectric profile $g(x,y)$ is given according to $\epsilon(x,y) = \epsilon_0(1+g(x,y))$. In this study, we assume that $g(x,y) = g_{0_1}$ in medium 2 and $g(x,y) = g_{0_2}$ in medium 4, where $g_{0_1} \neq g_{0_2}$.

III. The Proposed Model For The Helical Waveguide And The Technique For Solving The Cross Section

In this research, we will examine the influence on the output field of a helical waveguide with a rectangular cross section composed of several circular dielectric and hollow layers (Fig. 1(b)). We will use the method outlined in [4] for the helical waveguide, with the addition of the specific case of the cross section (Fig. 1(b)).

The mode model method is based on Maxwell's equations for the computation of output fields at each point along a curved waveguide. The method is based on Laplace and Fourier transforms and their inverse transforms. The following outlines the mathematics of the four-step solution.

Step 1: Application of the Laplace transform. The process begins by applying the Laplace transform to the vector wave equations in the ζ-direction (the axis of propagation). This transform is preferred because it explicity incorporates the initial conditions (the field profile at the waveguide entrance, ζ=0) into the equation. The Laplace transform facilitates the convenient and simple formulation of the field's input-output relations. The Laplace formulations are then tranfered to the s-plane.

Step 2: Fourier transform and spatial discretization. Next, a two-dimensional Fourier transform is performed on the transverse dimensions (x,y). The arbitrary dielectric profile g(x,y) and its derivatives are transformed into Fourier coefficients. The product of the dielectric profile and the fields in the spatial domain becomes a convolution operation in the Fourier domain. This is represented numerically by a cyclic matrix G, as shown in Appendix B. The continuous transverse wavenumber space is discretized into fundamental wavenumbers $k_{0x} = pi/a$ and $k_{0y} = pi/b$, effectively creating a "Fourier plane" where all subsequent calculations occur. The method yields Fourier coefficients of the transverse dielectric profile and of the input-output profile. In Laplace-Fourier space, the equations are entirely algebraic. The system is solved to find the output field vectors (E_x, E_y, E_z) as a function of the input field vectors and the dielectric properties, as explained in Appendix A.

Step 3: Inverse Laplace transform via Salzer method. To return to the physical ζ-dimension an inverse Laplace transform must be performed. The integration is carried out using a direct numerical integration (Gaussian quadrature) on the s-plane. Instead of finding individual poles or eigenmodes, the Salzer method uses specific weights (w_i) and zeros (p_i) of orthogonal polynomials to approximate the integral. This "robust solution" saves significant computational effort compared to eigenmode decomposition.

The inverse Laplace transform in the s-plane was proposed by Salzer [26,27]. While a standard inverse Laplace transform is often solved using partial fraction expansion or the Bromwich integral, Salzer's approach focuses on "quadrature formulas". This is particularly useful when the function F(s) is too complex for analytical inversion and requires a computational solution. While the Laplace transform is often used for transient systems, the inverse Fourier transform is the tool of choice for reconstructing signals from the frequency domain back into the time domain.

Step 4: Inverse Fourier transform to normal space. Finally, an inverse Fourier transform is applied to the calculated spatial spectrum. This step translates the coefficients from the Fourier domain back into the normal spatial domain, the final output results are given in the visual transverse-field profile (amplitude and phase) at the specific waveguide length L.

In summary, the four steps are: Laplace transform along the propagation axis, 2D Fourier transform across the transverse plane, algebraic solution in the transform domain, and numerical inversion via the Salzer quadrature method yielding the transverse electric field distribution at the rectangular helical waveguide output.

The output transverse field profiles are computed by the inverse Laplace and Fourier transforms. We will use the previously published development of a helical waveguide model [4], and the output components of the electric field are given finally in Appendix A. The equations describe the transfer relations between the spatial spectrum components of the output and input waves in the dielectric waveguide, and similarly, the other components of the magnetic field are obtained.

The resulting system of linear equations in the transform domain is solved using the ZGESV subroutine from the LAPACK library [28].

We will develop the proposed technique for solving the specific geometry of the cross section of the helical waveguide (Fig. 1(b)). The proposed technique enables the solution of problems with complex cross sections, such as the rectangular helical waveguide in Fig. 1, that cannot be solved using traditional analytical methods.

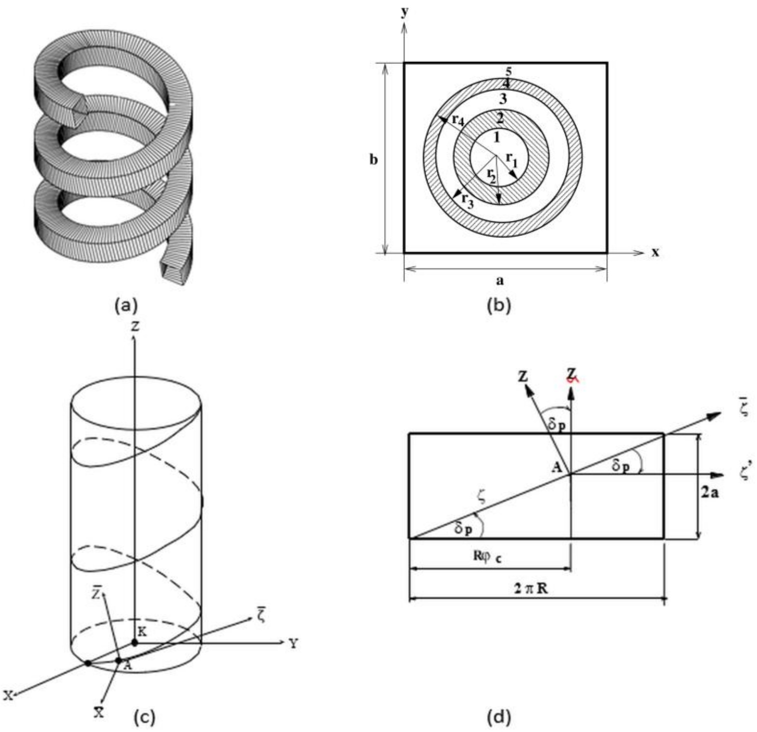

Figure 1: (a) The helical waveguide. (b) The cross section. (c). The axes and the coordinate along the helix axis ζ. (d) The deployment of the helix

In accordance with the model of the helical waveguide [4], we note that from the convolution operation we obtain a matrix form as $\boldsymbol{G}E$, where $\bar{g}(n,m)(n^{'},m^{'}) = g_{n-n^{'},m-m^{'}}$ and the matrix order is defined as (2N+1)(2M+1), where N and M determine the size of the cyclic matrix G used to represent the dielectric profile and the electric fields. In this study we assume N=M, so that the number of modes is $(2N+1)^2$.

The cyclic matrix $\boldsymbol{G}$ is shown in Appendix B, and consists of Fourier components of the dielectric profile $\bar{g}_{nm}$. In addition, the $\boldsymbol{G_x}$ and $\boldsymbol{G_y}$ matrices are obtained by the derivatives of the Fourier components of the dielectric profile, in accordance with the method described above. In order to calculate these matrices, the proposed method maps the physical geometry into a solvable domain before applying inverse transforms to obtain the final field distribution.

We now outline the precise technique that accommodates the comlex and challenging geometry in Fig. 1(b). We use the following technique to calculate the elements of the matrices for the specific cross section of the helical waveguide. For one circular dielectric layer and for $g(x,y) = g_0$, we obtain

$$g(n,m) = \frac{g_0}{4ab}\int_{-a}^{a} d\,x \int_{-b}^{b} \exp\left[-j(k_x x + k_y y)\right] dy = \frac{g_0}{4ab}\{J_1 + J_2 + J_3 + J_4\}, \quad (3a)$$

where,

$$J_1 = \int_{x_{11}}^{x_{12}} d\,x \int_{y_{11}}^{y_{12}} e\,xp\left[-j(k_x x + k_y y)\right] dy,$$

$$J_2 = \int_{-x_{12}}^{-x_{11}} d\,x \int_{y_{11}}^{y_{12}} \exp\left[-j(k_x x + k_y y)\right] dy,$$

$$J_3 = \int_{-x_{12}}^{-x_{11}} d\,x \int_{-y_{12}}^{-y_{11}} \exp\left[-j(k_x x + k_y y)\right] dy,$$

and

$$J_4 = \int_{x_{11}}^{x_{12}} d\,x \int_{-y_{12}}^{-y_{11}} \exp\left[-j(k_x x + k_y y)\right] dy,$$

where $k_x = (n\pi)/a$, and $k_y = (m\pi)/b$.

Thus, we obtain

$$g(n,m) = \frac{g_0}{2ab}\left\{\int_{x_{11}}^{x_{12}} (\exp(jk_x x) + \exp(-jk_x x))\, dx \int_{y_{11}}^{y_{12}} \cos(k_y y) dy\right\}$$
$$= \frac{g_0}{ab}\left\{\int_{x_{11}}^{x_{12}} \cos(k_x x) dx \int_{y_{11}}^{y_{12}} \cos(k_y y) dy\right\}, \qquad (3b)\ .$$

The dielectric profile is given by $\epsilon(x,y) = \epsilon_0(1 + g(x,y)$, and the derivatives of the dielectric profile are calculated according to

$$g_x(x,y) = \frac{1}{\epsilon(x,y)}\frac{d\epsilon(x,y)}{dx} \qquad (4a)\ ,$$

and

$$g_y(x,y) = \frac{1}{\epsilon(x,y)}\frac{d\epsilon(x,y)}{dy} \qquad (4b)\ .$$

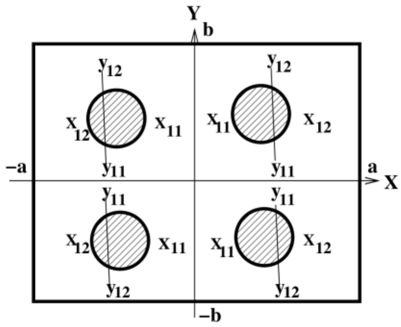

Figure 2: The described technique corresponds to the image method for each of the four radii (r_1, r_2, r_3, and r_4) of the specific cross section of the helical rectangular waveguide, as shown in Fig. 1(b)

The proposed technique corresponds to the image method for each of the four radii of the specific cross section (periodic replication). The periodic replication satisfies the metallic boundary conditions of the waveguide wall using the image method for each of the four layer radii, as shown in Fig. 2. Periodicity and symmetry properties are chosen to force the boundary conditions at the location of the walls in a real problem, by extending the waveguide region ($0 \le x \le a$, and $0 \le y \le b$) to four fold larger regions ($-a \le x \le a$, and $-b \le y \le b$).

Similarly, the geometry shown in Fig. 1(b) is based on the image method, according to the same principle as described in Fig. 2. The dielectric profile for the specific cross-section (Fig. 1(b)) is calculated for each of the four radii, where y_{11} and y_{12} are functions of x. Therefore

$$g(n,m) = \frac{g_0}{abk_y}\int_{x_{11}}^{x_{12}} \left[\sin(k_y y_{12}(x)) - \sin(k_y y_{11}(x))\right]\cos(k_x x) dx$$
$$= \frac{2g_0}{am\pi}\int_{x_{11}}^{x_{12}} \sin\left[\frac{m\pi}{2b}(y_{12}(x) - y_{11}(x))\right]\cos\left[\frac{m\pi}{2b}(y_{12}(x) + y_{11}(x))\right]\cos\left(\frac{n\pi}{a}x\right) dx. \qquad (5)$$

The radius for each of the four circles is given by

$$r_{1,2,3,4} = \sqrt{(x_{1,2,3,4} - a/2)^2 + (y_{1,2,3,4} - b/2)^2}. \qquad (6a,b,c.d)$$

Thus for each of the four radii of the cross section in Fig.1(b), we obtain

$$(y_{11})_{1,2,3,4} = b/2 - \sqrt{r_{1,2,3,4}^2 - (x_{1,2,3,4} - a/2)^2}, \quad (y_{12})_{1,2,3,4} = b/2 + \sqrt{r_{1,2,3,4}^2 - (x_{1,2,3,4} - a/2)^2}. (7a,b,c,d)$$

The dielectric profile for the specific cross section with the two circular dielectric layers in Fig. 1b is given for each of the four radii by

$$g_{1,2,3,4}(n,m \ne 0) = \frac{2g_0}{am\pi}\int_{x_{11}}^{x_{12}} \sin\left[\frac{m\pi}{2b}\left(y_{12}(x) - y_{11}(x)\right)\right]\cos\left[\frac{m\pi}{2b}\left(y_{12}(x) + y_{11}(x)\right)\right]\cos\left(\frac{n\pi}{a}x\right) dx, \quad (8a)$$

and

$$g_{1,2,3,4}(n,m = 0) = \frac{g_0}{ab}\int_{x_{11}}^{x_{12}}\left(y_{12}(x) - y_{11}(x)\right)\cos\left(\frac{n\pi}{a}x\right) dx. \qquad (8b)$$

The dielectric profile for the geometry in Fig. 1(b) is calculated as a superposition of the two circular dielectric profile layers seen in the media 2 and 4. Therefore, the dielectric profile in media 2 is calculated by subtracting the dielectric profile in media 1 at radius r_1 from the dielectric profile in media 2 at radius r_2. In addition, the dielectric profile in media 4 is calculated by subtracting the dielectric profile in media 3 at radius r_3 from the dielectric profile in media 4 at radius r_4. This can be expressed as

$$g(n,m) = (g_2(n,m) - g_1(n,m)) + (g_4(n,m) - g_3(n,m)). \quad (9)$$

Similarly, the elements of the matrices for the derivatives of the dielectric profile are given as follows

$$g_x(n,m) = \frac{2}{am\pi}\int_{x_{11}}^{x_{12}} g_x\,(x,y)\sin\left[\frac{m\pi}{2b}\big(y_{12}(x) - y_{11}(x)\big)\right]$$
$$\cos\left[\frac{m\pi}{2b}(y_{12}(x) + y_{11}(x))\right]\cos\left(\frac{n\pi}{a}x\right)dx, \quad (10a)$$

and

$$g_y(n,m) = \frac{2}{am\pi}\int_{x_{11}}^{x_{12}} g_y\,(x,y)\sin\left[\frac{m\pi}{2b}\big(y_{12}(x) - y_{11}(x)\big)\right]$$
$$\cos\left[\frac{m\pi}{2b}(y_{12}(x) + y_{11}(x))\right]\cos\left(\frac{n\pi}{a}x\right)dx, \quad (10b)$$

where $g_x(x,y)$ and $g_y(x,y)$ are defined in Eqs. (4a) and (4b), respectively.

IV. Numerical results

In Appendix C, we compare the performance of our proposed model to that of the traditional analytical method presented in [29]. It is demonstrated that the results of both methods are in good agreement, while our proposed method converges very rapidly (after only three iterations). Hence, our method is clearly computationally efficient, and can provide stable results for complex geometries, as will be shown below.

This section demonstrates some examples to examine the effect of the helical waveguides with the specific cross section (Fig. 1(b)). The cross section composed of several circular dielectric and hollow layers. Referring to this figure, we examine the output field for TE_{10} mode. We use the notation for thickness of the two circular dielectric layers d_1=r_2-r_1, d_2=r_4-r_3, where $r_4 > r_3 > r_2 > r_1$. The examples will be demonstrated for ζ = 0.15 m and a=b=20 mm.

Figure 3 illustrates the relationship between the physical geometry of the helical waveguide and its efficiency in transmitting output power. This figure presents a graph of the output power transmission (T) (in normalized units) versus the inverse of the cylinder radius (1/R). Regarding the effect of the helix angle (δ_p), the graph shows multiple curves corresponding to different helix angles (δ_p =0.0, 0.2, 0.4, 0.6, 0.8, and 1.0), demonstrating that for any given radius R, the output power transmission is highest when the helix angle is largest (δ_p=1). Regarding the effect of cylinder radius (R), for a fixed helix angle, the output power transmission increases as the radius R of the cylinder increases (i.e. lower values of 1/R). Conversely, decreasing the radius leads to a drop in output power transmission.

Note that when δ_p=0, the helical waveguide (in three-dimensional space) becomes a toroidal waveguide (in a plan), which is a special case.

The primary contribution of Fig. 3 is to provide a visual tool for optimizing the helical waveguide. It enables us to select the specific combinations of δ_p and R to achieve desired output results.

Figure 3 demonstrates for ζ = 0.15 m, δ_p =0.0, 0.2, 0.4, 0.6, 0.8, and 1.0. The other rest data are a=b=20 mm, ϵ_{r1} =8, ϵ_{r2} =4, r_1=1.1 mm, r_2=2.9 mm, r_3=3.3 mm, and r_4=4 mm, k_0 = 167 $1/m$, λ = 3.75 cm, and β = 58 $1/m$.

From the results in Fig. 3, we observe that the output power transmission increases as the cylinder radius (R) increases, and is maximized when the helix angle is at its largest (δ_p = 1.0). Therefore, in the following examples we will take the parameter δ_p = 1.0, to obtain results with high power transmission.

Figure 4 demonstrates the results of the helical waveguide for TE_{10} mode for R=26.5 mm, δ_p = 1.0, and ϵ_{r2} = 2, for the radii r_1 = 1.1 mm, r_2 = 2.86 mm, r_3 = 3.3 mm, and r_4 =5 mm, where ϵ_{r1} = 2, 4, 6, 8, and 10, respectively, in Figs. 4(a), (b), (c), (d), and (e). The output field for the results of Figs. 4(a)-(e) for the x-axis where y=0.5b=10 mm are shown in Fig. 4(f) for ϵ_{r1} = 2, 4, 6, 8, and 10.

From the results in Fig. 4 we observe that as the parameter ϵ_{r1} is increased from 2 to 10, the amplitude of the output field decreases, the width at half-height decreases, and the output profile becomes more Gaussian. Note that for ϵ_{r1}=2 (Fig.4(a)), the half-sine profile of the TE_{10} mode is more dominant than the output Gaussian profile. In contrast, for ϵ_{r1}=4, 6, 8, 10, the Gaussian shape is more dominant than the half-sine of the TE_{10} mode.

Figure 5 demonstrates the results of the helical waveguide for the same data as given in Fig. 4, but for the parameter of ϵ_{r2} = 4. In this case, Fig. 5(a) shows that the Gaussian shape is more dominant for the TE_{10}

mode, relative to the result shown in Fig. 4(a). In all other graphical results shown in Figs. 5(b)-(e), the Gaussian profile is more dominant than the graphical results shown in Figs. 4(b)-(e).

The two thicknesses of the two circular dielectric layers shown in Fig. 1(b) are given by d_1=r_2-r_1, and d_2=r_4-r_3. The examples shown in Figs. 4(a)-(f) and Figs. 5(a)-(f) are for thick dielectric layers, where d_1=1.75 mm and d_2=1.67 mm.

In contrast, in the results shown in Figs. 6(a)-(f) and 7(a)-(f) we only reduce the two circular dielectric layers, so that d_1=0.36 mm and d_2=0.67 mm. Except for the reduction in the thicknesses d_1 and d_2, all the other parameters in Figs. 6(a)-(f) are the same as in Figs. 4(a)-(f). Also, except for the reduction of the thicknesses d_1 and d_2, all the other parameters in Figs. 7(a)-(f) are the same as in Figs. 5(a)-(f).

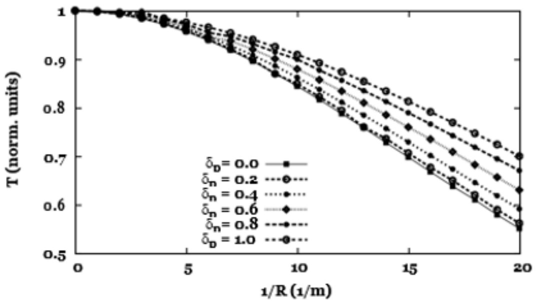

Figure 3: The effect of the output power transmission on 1/R in normalized units, where R is the radius of the cylinder. This example applies for ζ = 0.15 m, δ_p =0.0, 0.2, 0.4, 0.6, 0.8, and 1.0, a=b=20 mm, ϵ_{r1} =8, ϵ_{r2} =4, r_1=1.1 mm, r_2=2.9 mm, r_3=3.3 mm, and r_4=4 mm.

Figure 6 demonstrates the results of the helical waveguide for TE_{10} mode for R=26.5 mm, δ_p = 1.0, and ϵ_{r2} = 2, for the radii r_1 = 2.5 mm, r_2 = 2.86 mm, r_3 = 3.3 mm, and r_4 =4mm, where ϵ_{r1} = 2, 4, 6, 8, and 10, respevtively, in Figs. 6(a), (b), (c), (d), and (e). The output results of Figs. 6(a)-(e) for the x-axis where y=0.5b=10 mm are shown in Fig. 6(f) for ϵ_{r1} = 2, 4, 6, 8, and 10. The rest data are k_0 = 167 $1/m$, λ = 3.75 cm, and β = 58 $1/m$.

Figure 7 demonstrates the results of the helical waveguide for the same data as given in Fig. 6, but for the parameter of ϵ_{r2} = 4. In this case, Fig. 7(a) shows that the Gaussian shape is more dominant for the TE_{10} mode, relative to the result shown in Fig. 6(a). In all other graphical results shown in Figs. 7(b)-(e), the Gaussian profile is more dominant than in the graphical results shown in Figs. 6(b)-(e).

Note that:

(a). It is evident from Fig. 4 and Fig. 5 that as ϵ_{r1} increases, the field amplitude and width at half-height decrease, and the wave profile transitions from a traditional TE_{10} half-sine wave into a highly dominant Gaussian shape. Bending introduces an asymmetric shift in the cross-section.

(b). It appears that Fig. 6 and Fig. 7 exhibit similar evaluation structure as Fig. 4 and Fig. 5, but a closer look reveals the effects of thinner dielectric layers (d_1=0.36 mm, d_2=0.67 mm). These figures show that reducing the thickness changes the dominance of the Gaussian shape vs the half-sine wave, although increasing ϵ_{r2} to 4 makes the Gaussian profile significantly more pronounced. They also display the distinct asymmetric peak shift characteristic of curved waveguides.

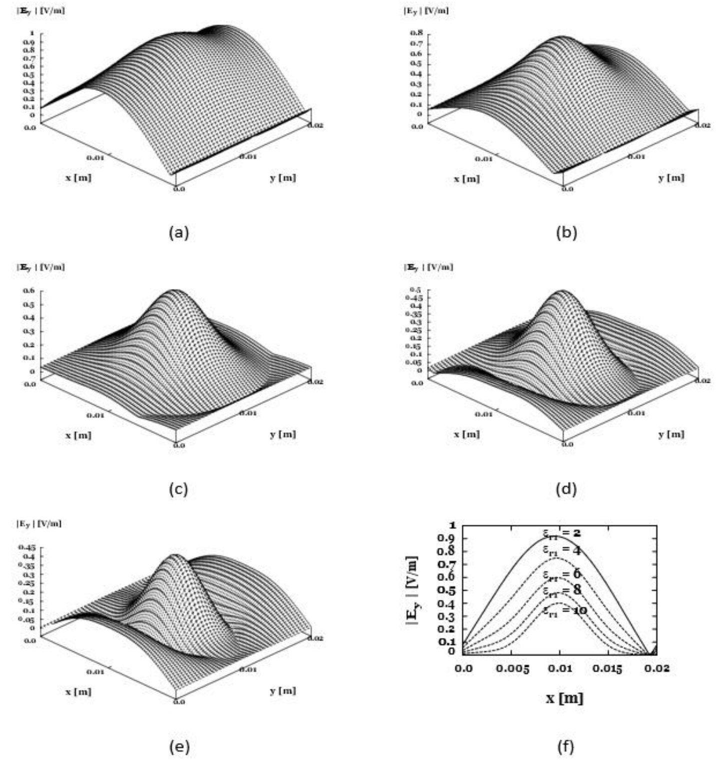

Figure 4: The effect of the transverse field at the output of the helical waveguide for TE_{10} mode for R=26.5 mm, δ_p = 1.0, ϵ_{r2} = 2, for the radii r_1 = 1.1 mm, r_2 = 2.86 mm, r_3 = 3.3 mm, and r_4 = 5 mm, in the cases: (a) ϵ_{r1} = 2 ; (b) ϵ_{r1} = 4; (c) ϵ_{r1} = 6; (d) ϵ_{r1} = 8 and (e) ϵ_{r1} = 10; (f) the output field for the results (a)-(e) for the x-axis, where y=0.5b=10 mm

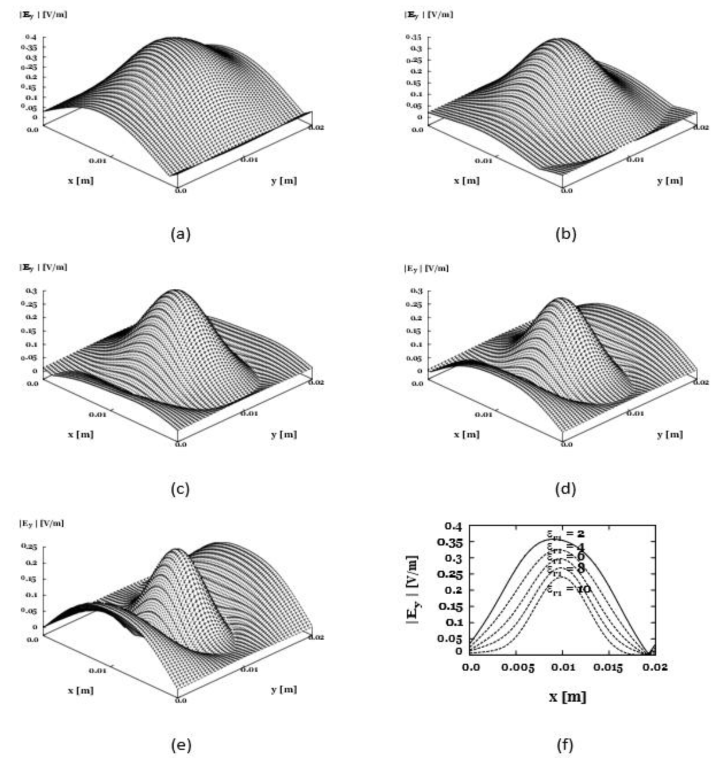

Figure 5: The effect of the transverse field at the output of the helical waveguide for TE_{10} mode for R=26.5 mm, δ_p = 1.0, ϵ_{r2} = 4, for the radii r_1 = 1.1 mm, r_2 = 2.86 mm, r_3 = 3.3 mm, and r_4 = 5 mm, in the cases: (a) ϵ_{r1} = 2 ; (b) ϵ_{r1} = 4; (c) ϵ_{r1} = 6; (d) ϵ_{r1} = 8 and (e) ϵ_{r1} = 10; (f) the output field for the results (a)-(e) for the x-axis, where y=0.5b=10 mm

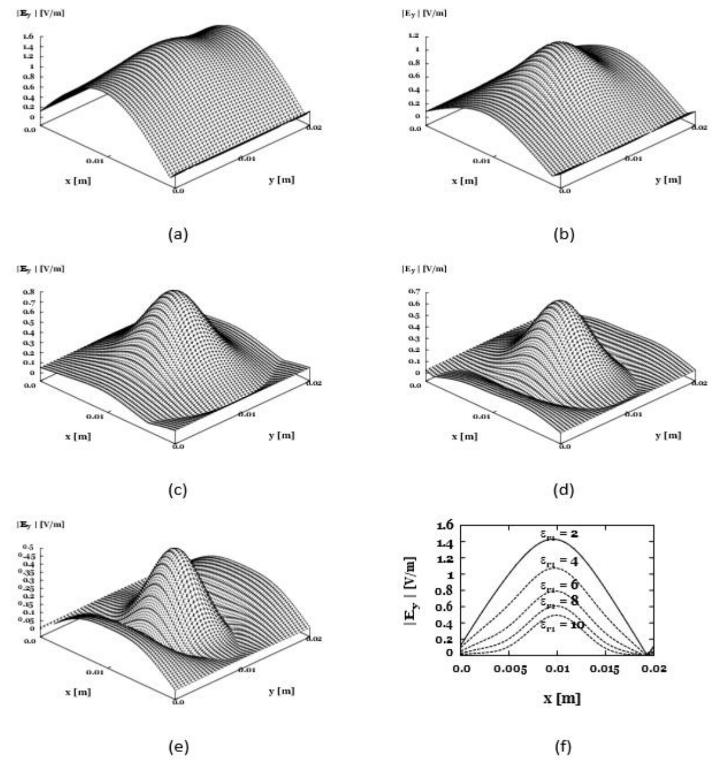

Figure 6: The effect of the transverse field at the output of the helical waveguide for TE_{10} mode for R=26.5 mm, δ_p = 1.0, ϵ_{r2} = 2, for the radii r_1 = 2.5 mm, r_2 = 2.86 mm, r_3 = 3.3 mm, and r_4 = 4 mm, in the cases: (a) ϵ_{r1} = 2 ; (b) ϵ_{r1} = 4; (c) ϵ_{r1} = 6; (d) ϵ_{r1} = 8 and (e) ϵ_{r1} = 10; (f) the output field for the results (a)-(e) for the x-axis, where y=0.5b=10 mm

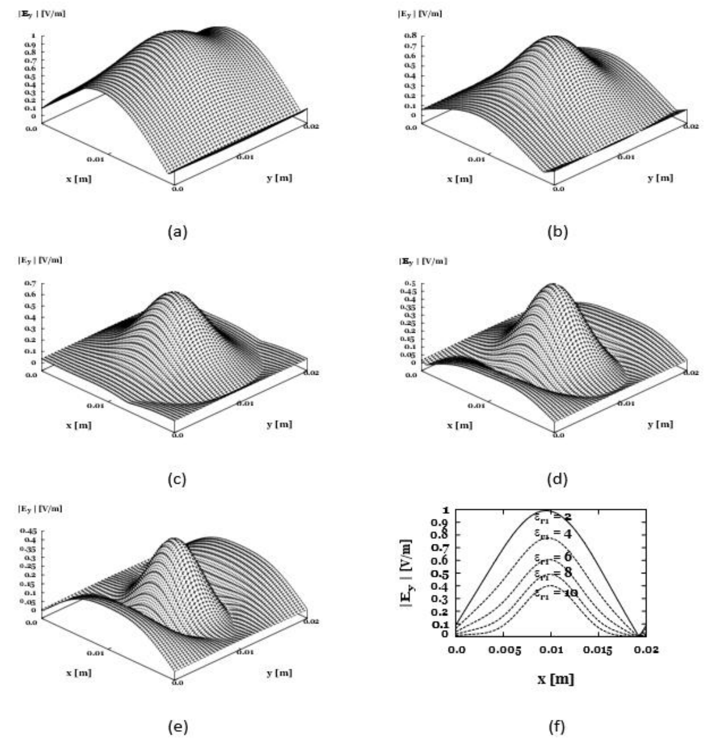

Figure 7: The effect of the transverse field at the output of the helical waveguide for TE_{10} mode for R=26.5 mm, δ_p = 1.0, ϵ_{r2} = 4, for the radii r_1 = 2.5 mm, r_2 = 2.86 mm, r_3 = 3.3 mm, and r_4 = 4 mm, in the cases: (a)

ϵ_{r1} = 2 ; (b) ϵ_{r1} = 4; (c) ϵ_{r1} = 6; (d) ϵ_{r1} = 8 and (e) ϵ_{r1} = 10; (f) the output field for the results (a)-(e) for the x-axis, where y=0.5b=10 mm

For bending problems, we obtain asymmetric behavior in the cross-section, as seen in the graphical results in Figs. 4(f), 5(f), 6(f), and 7(f). These results are expected, because the output profile of the wave propagation with respect to the ζ axis and the relative bending with respect to a straight waveguide causes a shift of the output profile in the cross section.

V. Conclusions

This research presents a method for computing electromagnetic field propagation in a helical waveguide whose rectangular cross-section consists of alternating circular dielectric and hollow layers (Fig. 1(b)). The main goal of this study was to examine the behavior of the output fields in this interesting and challenging case. The helical geometry is described using a coordinate transformation involving two rotations and a translation, parameterized by the cylinder radius R and the helix angle δ_p.

The relationship between the physical geometry of the helical waveguide and its efficiency in transmitting output power is illustrated in Fig. 3 in terms of the output power transmission versus the inverse of the cylinder radius.

We further observe that for a given radius, the output power transmission is highest when the helix angle is largest. Regarding the effect of helix angle, the graph shows multiple curves corresponding to different helix angles (δ_p =0.0, 0.2, 0.4, 0.6, 0.8, and 1.0). Regarding the effect of cylinder radius (R), for a fixed helix angle, output power transmission increases as the radius R of the cylinder increases. In this paper, we have provided a visual tool for optimizing the helical waveguide. It enables us to select the specific combinations of δ_p and R to achieve desired output results.

By increasing the dielectric profile ϵ_{r1} from 2 to 10, the amplitude of the field at the exit decreases, the width at half-height decreases, and the output profile becomes more Gaussian. For ϵ_{r1}=2 (Fig.4(a)), the half-sine profile of the TE_{10} mode is more dominant than the output Gaussian shape. In contrast, for ϵ_{r1}=4, 6, 8, 10, the Gaussian shape is more dominant than the half-sine of the TE_{10} mode. By changing the parameter ϵ_{r2} from 2 to 4, while keeping the other parameters unchanged, we observe that the Gaussian shape is more dominant than the results shown in Figs. 4(a)-4(e).

From the results in Fig. 4 we observe that as the parameter ϵ_{r1} is increased from 2 to 10, the amplitude of the output field decreases, the width at half-height decreases, and the output profile becomes more Gaussian. Note that for ϵ_{r1}=2 (Fig.4(a)), the half-sine profile of the TE_{10} mode is more dominant than the output Gaussian profile. In contrast, for ϵ_{r1}=4, 6, 8, 10, the Gaussian shape is more dominant than the half-sine of the TE_{10} mode.

Figure 5 demonstrates the results of the helical waveguide for the same data as given in Fig. 4, but for the parameter of ϵ_{r2} = 4. In this case, Fig. 5(a) shows that the Gaussian shape is more dominant for the TE_{10} mode, relative to the result shown in Fig. 4(a). In all other graphical results shown in Figs. 5(b)-(e), the Gaussian profile is more dominant than the graphical results shown in Figs. 4(b)-(e).

The two thicknesses of the two circular dielectric layers shown in Fig. 1(b) are given by d_1=r_2-r_1, and d_2=r_4-r_3. The examples shown in Figs. 4(a)-(f) and Figs. 5(a)-(f) are for thick dielectric layers, where d_1=1.75 mm and d_2=1.67 mm.

In contrast, in the results shown in Figs. 6(a)-(f) and 7(a)-(f) we only reduce the two circular dielectric layers, so that d_1=0.36 mm and d_2=0.67 mm. Except for the reduction in the thicknesses d_1 and d_2, all the other parameters in Figs. 6(a)-(f) are the same as in Figs. 4(a)-(f). Also, except for the reduction of the thicknesses d_1 and d_2, all the other parameters in Figs. 7(a)-(f) are the same as in Figs. 5(a)-(f).

For bending problems, we obtain asymmetric behavior in the cross-section, as seen in the graphical results in Figs. 4(f), 5(f), 6(f), and 7(f). These results are expected, because the output profile of the wave propagation with respect to the ζ axis and the relative bending with respect to a straight waveguide causes a shift of the output profile in the cross section.

The results presented in this paper can be helpul for the development of advanced systems relating to the helical waveguide contains multiple circular dielectric and hollow layers, for the microwave regime.

Appendix A

The output transverse field profiles are computed by the inverse Laplace and Fourier transforms. The output components of the electric field according to Re.[4] are given by

$$E_x = \left\{ \boldsymbol{D_x} + \alpha_1 \boldsymbol{Q^{(1)}} \boldsymbol{M_1} \boldsymbol{Q^{(1)}} \boldsymbol{M_2} + \frac{1}{R}\cos^2(\delta_p)\boldsymbol{D_\zeta}^{-1}(-\frac{1}{2}\boldsymbol{Q^{(1)}}\boldsymbol{G_x} + \frac{1}{2}\alpha_2 \boldsymbol{Q^{(1)}}\boldsymbol{M_3}\boldsymbol{Q^{(1)}}\boldsymbol{M_2} - \frac{1}{R}\cos^2(\delta_p)\boldsymbol{I}) \right\}^{-1}$$

$$(\hat{E}_{x_0} - \frac{1}{sR}\cos^2(\delta_p)E_{\zeta_0} - \alpha_3 \boldsymbol{Q^{(1)}}\boldsymbol{M_1}\hat{E}_{y_0} + \frac{1}{R}\cos^2(\delta_p)\boldsymbol{D_\zeta}^{-1}(\hat{E}_{\zeta_0} + \frac{1}{sR}\cos^2(\delta_p)E_{x_0} +$$

$$\frac{1}{2s}\boldsymbol{Q^{(1)}}(\boldsymbol{G_x}E_{x_0} + \boldsymbol{G_y}E_{y_0}) - \frac{1}{2}\boldsymbol{Q^{(1)}}\boldsymbol{M_3}\hat{E}_{y_0})), \quad \text{(A1a)}$$

$$E_y = \boldsymbol{D_y}^{-1}\left(\hat{E}_{y_0} - \frac{jk_{oy}}{2s}\boldsymbol{Q^{(1)}}\boldsymbol{M}\boldsymbol{G_x}E_x\right), \quad \text{(A1b)}$$

$$E_\zeta = \boldsymbol{D_\zeta}^{-1}\left\{\hat{E}_{\zeta_0} + \frac{1}{2s}\boldsymbol{Q^{(1)}}(\boldsymbol{G_x}E_{x_0} + \boldsymbol{G_y}E_{y_0}) - \frac{1}{2}\boldsymbol{Q^{(1)}}(\boldsymbol{G_x}E_x + \boldsymbol{G_y}E_y) - \frac{1}{R}\cos^2(\delta_p)E_x + \frac{1}{sR}\cos^2(\delta_p)E_{x_0}\right\}, \quad \text{(A1c)}$$

where E_{x_0}, E_{y_0}, $E_{\zeta 0}$ are the initial values of the corresponding fields at $\zeta = 0$, i.e. $E_{x_0} = E_x(x, y, \zeta = 0)$ and $E'_{x_0} = \frac{\partial}{\partial \zeta}E_x(x, y, \zeta)|_{\zeta=0}$,

$$\alpha_1 = \frac{k_{ox}k_{oy}}{4s^2}, \quad \alpha_2 = \frac{jk_{oy}}{2s}, \quad \alpha_3 = \frac{jk_{ox}}{2s}, \quad \boldsymbol{M_1} = \boldsymbol{N}\boldsymbol{G_y}\boldsymbol{D_y}^{-1}, \quad \boldsymbol{M_2} = \boldsymbol{M}\boldsymbol{G_x}, \quad \boldsymbol{M_3} = \boldsymbol{G_y}\boldsymbol{D_y}^{-1}.$$

The elements of the diagonal matrices $\boldsymbol{K^{(0)}}$, $\boldsymbol{M}$, $\boldsymbol{N}$ and $\boldsymbol{K^{(1)}}$ are defined as

$$K^{(0)}{}_{(n,m)(n',m')} = \{[k_o^2 - (n\pi/a)^2 - (m\pi/b)^2 + s^2]/2s\}\delta_{nn'}\delta_{mm'},$$

$$M_{(n,m)(n',m')} = m\delta_{nn'}\delta_{mm'},$$

$$N_{(n,m)(n',m')} = n\delta_{nn'}\delta_{mm'},$$

$$K^{(1)}{}_{(n,m)(n',m')} = \{[k_o^2 - (n\pi/a)^2 - (m\pi/b)^2]/2s\}\delta_{nn'}\delta_{mm'}.$$

where $\delta_{nn'}$ and $\delta_{mm'}$ are the Kronecker delta functions.

The modified wave-number matrices are defined as

$$\boldsymbol{D_x} \equiv \boldsymbol{K^{(0)}} + \boldsymbol{Q^{(0)}}\boldsymbol{K1^{(0)}} + \frac{k_o^2\chi_0}{2s}\boldsymbol{Q^{(1)}}\boldsymbol{G} + \frac{jk_{ox}}{2s}\boldsymbol{Q^{(1)}}\boldsymbol{N}\boldsymbol{G_x} + \frac{1}{2sR}\cos^2(\delta_p)jk_{ox}\boldsymbol{P^{(1)}}\boldsymbol{N},$$

$$\boldsymbol{D_y} \equiv \boldsymbol{K^{(0)}} + \boldsymbol{Q^{(0)}}\boldsymbol{K1^{(0)}} + \frac{k_o^2\chi_0}{2s}\boldsymbol{Q^{(1)}}\boldsymbol{G} + \frac{1}{2sR}\cos^2(\delta_p)jk_{ox}\boldsymbol{P^{(1)}}\boldsymbol{N} + \frac{jk_{oy}}{2s}\boldsymbol{Q^{(1)}}\boldsymbol{M}\boldsymbol{G_y},$$

$$\boldsymbol{D_\zeta} \equiv \boldsymbol{K^{(0)}} + \boldsymbol{Q^{(0)}}\boldsymbol{K1^{(0)}} + \frac{k_o^2\chi_0}{2s}\boldsymbol{Q^{(1)}}\boldsymbol{G} + \frac{1}{2sR}\cos^2(\delta_p)jk_{ox}\boldsymbol{P^{(1)}}\boldsymbol{N}.$$

Equations A1(a)-(c) describe the transfer relations between the spatial spectrum components of the output and input waves in the dielectric waveguide. Similarly, the other components of the magnetic field can be obtained. The transverse field profiles are computed by the inverse Laplace and Fourier transforms, as follows

$$E_y(x, y, \zeta) = \sum_n \sum_m \int_{\sigma - j_\infty}^{\sigma + j_\infty} E_y\,(n, m, s)e^{jnk_{ox}x + jmk_{oy}y + s\zeta}ds. \quad \text{(A2)}$$

The inverse Laplace transform is performed in this study by a direct numerical integration on the s-plane by the method of Gaussian Quadrature. The integration path on the right side of the s-plane includes all the singularities, as proposed by Salzer [26]-[27]

A Fortran code was developed using NAG subroutines (The Numerical Algorithms Group (NAG)) [28].

Appendix B

The cyclic matrix $\boldsymbol{G}$ is given as follows. The Fourier transform is applied on the transverse dimension

$$\bar{g}(k_x, k_y) = \mathcal{F}\{g(x, y)\} = \int_x \int_y g\,(x, y)e^{-jk_x x - jk_y y}dxdy. \quad \text{(B1)}$$

The components are organized in a vectorial notation as follows

$$\boldsymbol{E} = \begin{bmatrix} \bar{E}_{-N,-M} \\ ;\vdots \\ ;\bar{E}_{-N,+M} \\ ;\vdots \\ ;\bar{E}_{+n,+m} \\ \vdots \\ ;\bar{E}_{+N,+M} \\ ; \end{bmatrix}. \quad \text{(B2)}$$

The Fourier components of the dielectric profile are calculated in the Fourier space. The convolution operation

$$\bar{g} * \bar{E} = \left\{\sum_{n'=-N}^{N} \sum_{m'=-M}^{M} g_{n-n',m-m'} E_{n',m'}\right\} \tag{B3}$$

is written in a matrix form as $\boldsymbol{G}E$, where

$$\bar{g}(n,m)(n',m') = g_{n-n',m-m'}. \tag{B4}$$

The matrix order is specifically defined as (2N+1)(2M+1), where N and M determine the size of the cyclic matrix G used to represent the dielectric profile and the electric fields. The number of the modes is equal to $(2N+1)^2$, for N=1, 3, 5, 7 , 9, and E is the electric field.

The convolution operation is expressed by the cyclic matrix $\boldsymbol{G}$ which consists of Fourier components of the dielectric profile $\bar{g}_{nm}$. Thus, the cyclic matrix $\boldsymbol{G}$ is given by the form

$$\boldsymbol{G} = \begin{bmatrix} g_{00} & g_{-10} & g_{-20} & \cdots & g_{-nm} & \cdots & g_{-NM} \\ g_{10} & g_{00} & g_{-10} & \cdots & g_{-(n-1)m} & \cdots & g_{-(N-1)M} \\ g_{20} & g_{10} & \ddots & \ddots & & & \ddots \\ \vdots & g_{20} & \ddots & \ddots & & & \ddots \\ g_{nm} & \ddots & \ddots & \ddots & g_{00} & & \vdots \\ \vdots & & & & & & \\ g_{NM} & \cdots & \cdots & \cdots & \cdots & \cdots & g_{00} \end{bmatrix}. \tag{B5}$$

Appendix C

Figure 8(a) illustrates the physical slab profile in the cross section of a rectangular straight waveguide, which is used for comparison. The cross-section consists of three inhomogeneous regions. This profile is based on a transcendental equation used in the traditional analytical method [29].

Figures 8(a) and 8(b) serve to validate and verify the accuracy of the proposed theoretical model against the analytical model [29]. The number of the modes is equal to $(2N+1)^2$, for N=1, 3, 5, 7 , 9. Namely, the number of the modes is equal to 9, 49, 121, 225, and 361, respectively.

The comparison give us good agreement. Our numerical model allows for rapid convergence after only three iterations even if it cannot be compared to another known model, and this is considered a great advantage.

The parameters in our example are: a= 20 mm, b=10 mm, d=3.3 mm, t=8.35 mm, $\epsilon_r = 9$, and $\lambda =$ 6.9 cm.

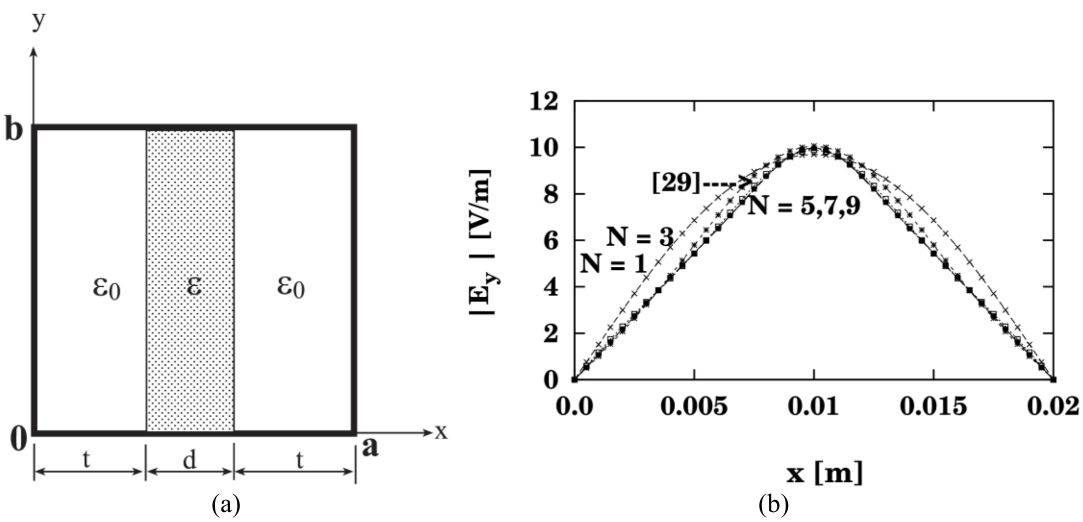

Figure 8: (a) Cross section (b) Comparison with the transcendental equation [29]

$$E_y = \begin{cases} j\dfrac{k_z}{\epsilon_0}\sin(\nu x) & 0 < x < t \\ j\dfrac{k_z}{\epsilon_0}\dfrac{\sin(\nu t)}{\cos(\mu(t-a/2))}\cos[\mu(x-a/2)] & t < x < t+d \\ j\dfrac{k_z}{\epsilon_0}\sin[\nu(a-x)] & t+d < x < a \end{cases}$$

where $\nu \equiv [k_o^2 - k_z^2]^{1/2}$ and $\mu \equiv [\epsilon_r k_o^2 - k_z^2]^{1/2}$.

Figure 8(b) shows that $E_y(N = 5)$ already approaches to the result E_y of the analytical solution [29] with good agreement. Since our model converges in only three iterations, it is clearly computationally efficient and provides stable results even for complex geometries that cannot be compared to known modes.

References

[1] Marcatili, E. A. J., And R. A. Schmeltzer, "Hollow Metallic And Dielectric Waveguides For Long Distance Optical Transmission And Lasers," Bell Syst. Tech. J., Vol. 43, 1783-1809, 1964.

[2] Marhic, M. E., "Mode-Coupling Analysis Of Bending Losses In IR Metallic Waveguides", Appl. Opt., Vol. 20, 3436-3441, 1981.

[3] Miyagi, M., K. Harada And S. Kawakami, "Wave Propagation And Attenuation In The General Class Of Circular Hollow Waveguides With Uniform Curvature", IEEE Transactions On Microwave Theory And Techniques, Vol. MTT-32, 513-521, 1984.

[4] Menachem Z., "Effective Technique For Analyzing Rectangular Helical And Toroidal Waveguides With A Hollow Rectangle Bounded By Dielectrical Material And Metal Boundary", Journal Of Electromagnetic Waves And Applications, Vol. 36, 804-829, 2021.

[5] Andrea Melloni, Federico Carniel, Raffaella Costa, And Mario Martinelli, "Determination Of Bend Mode Characteristics In Dielectric Waveguides," J. Of Lightwave Technology, Vol. 19, 571-577, 2001.

[6] Peter Bienstman, M. Roelens, M. Vanwolleghem, And Roel Baets, "Calculation Of Bending Losses In Dielectric Waveguides Using Eigenmode Expansion And Perfectly Matched Layers," IEEE Photonics Letters, Vol. 14, 164-166, 2022.

[7] Hiremath, K. R. Hammer, M, Stoffer, R, Prkna, L, And Ctyroky,"Analytic Approach To Dielec-Tric Optical Bent Slab Waveguides," Optical And Quantum Electronics, 37(1), 37-61, 2005.

[8] Jinbiao Xiao And Xiaohan Sun, "Vector Analysis Of Bending Waveguides By Using A Modified Finite-Difference Method In A Local Cylindrical Coordinate System," Optics Express, Vol. 20, 21583-21597, 2012.

[9] Sabaina Irfan, Jae-Yong Kim, And Hamza Kurt, "Ultra-Compact And Efficient Photonic Waveg-Uide Bends With Different Configurations Designed By Topology Optimization," Scientific Rre-Ports, Vol. 14, 6453, 2024.

[10] Balwan Rana, And Mariana Dalarsson, "TE-Wave Propagation In A Hollow Circual Waveguide Filled With A Graded Multilayered Dielectric Medium," EPJ Appl. Metamat., Vol. 12, 1-9, 2025.

[11] Tigran Baghdasaryan, Neshteh Kourian, Mushegh Rafayelyan, And Tatevik Sarukhanyan, "Low-Loss Multimode Waveguide Bends With Direct Laser Writing In Polymer,"Micromachines, Vol. 16, 1361, 2025.

[12] Hao Li, Dehai Zhang, And Haotian Zhu, "PTFE-Based Circular Terahertz Dielectric Waveguides," Photonics, Vol. 11, 921, 2024.

[13] Michael Krause, "Finite-Difference Mode Solver For Curved Waveguides With Angled And Curved Dielectric Interfaces,"Journal Of Lightwave Technology, Vol. 29, 691-699, 2011.

[14] Saib Thiab Alwan, Abbas AI-Bawee, And Ahmed AAG Airubaiy, "Behavior Of TE And TM Propagation Modes In Nanomaterial Graphene Using Asymmetric Slab Waveguide,"Curved And Layered Structures, Vol. 11, 2024.

[15] Omar E. Eisheikh, Adel Shaaban, A. Arafa, Ashraf Yahya, Lotfy Rabeh Gomaa, And Nasr Gad, "Predicting Fundamental Transverse Electric Mode Of Slab Waveguide Based On Physics-Informed Neural Networks,"Egyptian Journal Of Pure And Applied Science, Vol. 61, 1-10, 2023.

[16] Xinya W., Xiaoming Yu., Matthew J.B., Pingping C., Brice L., Sasan F., And Shuting L., "Curved Waveguides In Silicon Written By A Shaped Laser Beam", Optics Express, Vol. 29, Pp. 14201-14207, 2021.

[17] Wei L., Hechao L., Xiaohong S., And Fan Z., "The Design Of Large Curved Waveguide Based On Sunflower Graded Photonic Crystal", Photonics, Vol. 10, Pp. 1-16, 2023.

[18] Celeste Q., Zhe L., Camille P., Andreas D.W., Arne L., And Leonardo M., "Curved Gaas Cantilever Waveguides For The Vertical Coupling To Photonic Integrated Circuits", Optics Express, Vol. 32, Pp. 3723-3734, 2024.

[19] Thiyagarajan J.S., "Elastic Guided Wave Propagation In The Prestressed Helical Multiwire Waveg-Uide", Journal Of Engineering Mechanics, Vol. 148, 2022.

[20] Guilherme S.R., "An Accurate And Numerically Stable Formulation For Computing The Electro-Magnetic Fields In Uniform Bend Rectangular Waveguides", IEEE Transactions On Microwave Theory And Techniques, Vol. 71, Pp. 988-996, 2022.

[21] Thomas G., Jean-Baptiste D., And Simon F., "Improved Multimodal Formulation Of The Wave Propagation In A 3D Waveguide With Varying Cross-Section And Curvature", The Journal Of The Acoustical Society Of America, Vol. 149, Pp. 476-486, 2021.

[22] Chia H.W., Zhenyu Q., Wei W., Jianqi S., Xianqing L., Li-Yi Z., Fang H., Xiaolong W., Zhuoyuan W., Song T.P., Guoning Z., Linfang S., Yun ., And Hang Z., "A Direct Near-Field Observation Of Conversion Between Waveguide Modes And Leaky Modes In Periodic Metal Struc-Tures", Journals And Magazines, Vol. 11, Pp. 16128-16141, 2023

[23] Darche M., Lopez-Caballero F., And Tie B., "Modal Analysis Of Waveguide For The Study Of Frequency Bandgaps Of A Bounded Periodic Medium", Journal Of Sound And Vibration, Vol. 572, 2024.

[24] Salem M., Kirolous H., And Abuelfadi T., "Analysis Of Periodic Waveguide Excitation With Arbitrary Shaped Corrugation", National Radio Science Conference, IEEE, Pp. 62-73, 2023.

[25] Ghahremani M., And Shahabadi M., "Accurate Characterization Of Complex Bloch Modes In Optical Chain Waveguides Using Real-Valued Computations", Scientific Reports, Vol. 13, P.22115, 2023.

[26] Salzer, H. E.,"Orthogonal Polynomials Arising In The Numerical Evaluation Of Inverse Laplace Transforms," Math. Tables And Other Aids To Comut., Vol. 9, 164-177, 1955.

[27] Salzer, H. E., "Additional Formulas And Tables For Orthogonal Polynomials Originating From Inversion Integrals," J. Math. Phys., Vol. 39, 72-86, 1961.

[28] The Numerical Algorithms Group (NAG) Ltd., Wilkinson House, Oxford, U.K. Subroutine ZGESV, 1970.

[29] Collin R.E., Foundation For Microwave Engineering, New York: Mcgraw-Hill, 1996.